NANOROBOTS

Robotic end-to-end fusion of microtubules powered by kinesin

Gadiel Saper[1], Stanislav Tsitkov[1], Parag Katira[2], Henry Hess[1]*

The active assembly of molecules by nanorobots has advanced greatly since "molecular manufacturing"—that is, the use of nanoscale tools to build molecular structures—was proposed. In contrast to a catalyst, which accelerates a reaction by smoothing the potential energy surface along the reaction coordinate, molecular machines expend energy to accelerate a reaction relative to the baseline provided by thermal motion and forces. Here, we design a nanorobotics system to accelerate end-to-end microtubule assembly by using kinesin motors and a circular confining chamber. We show that the mechanical interaction of kinesin-propelled microtubules gliding on a surface with the walls of the confining chamber results in a nonequilibrium distribution of microtubules, which increases the number of end-to-end microtubule fusion events 20-fold compared with microtubules gliding on a plane. In contrast to earlier nanorobots, where a nonequilibrium distribution was built into the initial state and drove the process, our nanorobotic system creates and actively maintains the building blocks in the concentrated state responsible for accelerated assembly through the adenosine triphosphate–fueled generation of force by kinesin-1 motor proteins. This approach can be used in the future to develop biohybrid or bioinspired nanorobots that use molecular machines to access nonequilibrium states and accelerate nanoscale assembly.

INTRODUCTION

The ribosome inspired the concept of molecular assemblers, which use energy-consuming processes to accelerate the assembly of molecular building blocks into larger structures (*1*, *2*). The first synthetic molecular assemblers used topologically linked catalysts to sequentially extend a polymer (*3*, *4*). Leigh and colleagues (*5*, *6*) designed rotaxanes that picked amino acids off a molecular strand as they traveled along and joined them into peptides of specific sequence and length. The driving force is entropy for the travel and an exothermic reaction for the peptide formation. Kassem *et al.* (*7*) created a pH-activated molecular switch that controllably selected from different reaction pathways, demonstrating the advances in designing molecular switches with fidelity, addressability, and robustness. Molecular assemblers can also be constructed with the tools of DNA nanotechnology (*8*, *9*), where assembly steps are thermodynamically driven.

Within molecular assemblers, building blocks diffusively cover Angstrom distances, and DNA nanorobots have been shown to diffusively or directedly traverse distances from nanometers (*10*–*12*) to micrometers (*13*). In contrast, biomolecular motors, such as the motor proteins kinesin or myosin, can transport their associated cytoskeletal filaments (microtubules and actin filaments) over micrometer to millimeter scales as they move and assemble them (*14*–*17*). The large distances greatly facilitate the direct observation of the assembly process using fluorescence microscopy. This, in turn, enables a focus on the assembly kinetics rather than a focus on the fidelity of the sequential execution of preprogrammed assembly steps (*5*–*11*).

One of the grand challenges in robotics is the design of biohybrid robots that integrate biological components with synthetic structures to perform complex tasks (Fig. 1) (*18*, *19*). Here, we take on this challenge and design a system containing kinesin biomolecular motors confined in a synthetic circular guiding structure to accelerate the end-to-end fusion of microtubules (Fig. 2A). End-to-end fusion of thin (25-nm diameter) and long (several micrometers) microtubules is much more sensitive to microtubule positioning and alignment than cross-linking along the microtubule lattice (*14*–*17*), making it an assembly process particularly suited to demonstrating molecular robotic assembly. The microtubules are propelled by the surface-adhered kinesins using the molecular fuel adenosine triphosphate (ATP), and their confinement drives the system to a high energy state where end-to-end fusion of microtubules occurs at an accelerated rate compared with the same system in the absence of confinement. The driving force for accelerated assembly is thus not a preselected high energy state accessed during the chemical synthesis of the assembler, but a nonequilibrium state emerging as a result of the dynamics of the dissipative system. Using the presented system as an example, we discuss general questions related to the capabilities of nanoscale robots.

RESULTS

Kinesin-propelled microtubules exhibit end-to-end fusion when confined in a circular chamber

The experimental model system used here to investigate the nanorobotic acceleration of assembly is the end-to-end fusing of microtubules (*20*–*23*). In contrast to microtubule assembly via the addition of tubulin dimers to the ends of microtubules, in end-to-end fusion, the plus end of one microtubule will attach to the minus end of a second microtubule (fig. S1). The end-to-end fusion is accelerated in a confining structure during microtubule gliding on a surface coated with kinesin-1 motor proteins. Microtubules propelled by surface-adhered full-length kinesin-1 motor proteins perform a persistent random walk (*24*, *25*) and cross each other without changing direction. Because of a low rate of well-aligned end-to-end collisions, assembly (or fusion) events are rarely observed. When the gliding motion of the microtubules is confined in a circular chamber (50-μm diameter and 0.5-μm height; Fig. 2B and fig. S2), the work done by the kinesin

[1]Department of Biomedical Engineering, Columbia University, New York, NY, USA. [2]Department of Mechanical Engineering, San Diego State University, San Diego, CA, USA.
*Corresponding author. Email: hh2374@columbia.edu

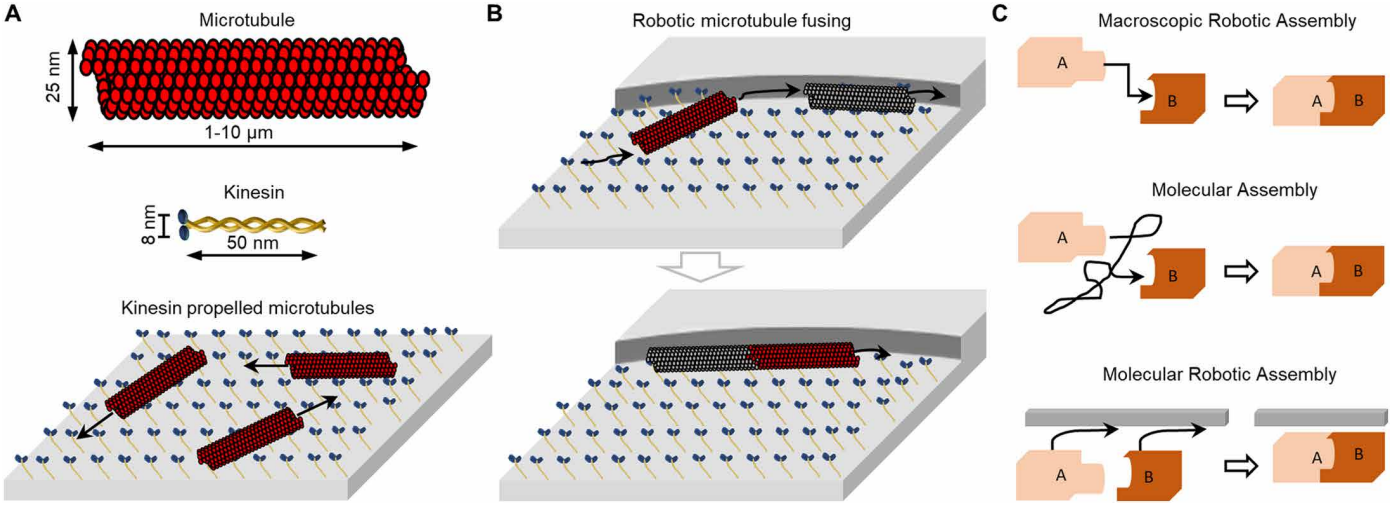

Fig. 1. Molecular robotic assembly powered by molecular motors. (**A**) Surface-adsorbed kinesin molecular motors can propel microtubules, cytoskeletal filaments assembled from tubulin proteins. (**B**) The kinesin motors together with guiding structures form a robot that manipulates microtubules, aggregating and aligning them to accelerate their end-to-end fusion. (**C**) Macroscopic robotic assembly aims to suitably manipulate immobile objects, molecular-scale objects often are mobile because of their thermal energy, and assembly can proceed spontaneously as a result of encounters between binding sites. Molecular robotic assembly can accelerate this process by guiding the building blocks toward configurations that facilitate assembly in an energy-consuming process.

motors leads to a nonequilibrium distribution of microtubules, because the microtubules begin to follow the boundary (Movie 1) (*26*). The increased density and alignment of microtubules lead to a fourfold increase in the average length of the microtubules within 20 hours and a shift in the length distribution toward longer microtubules (Fig. 2, C to E).

The key to confining microtubules in a flat circular chamber is the Convex Lens–induced Confinement (CLiC) device (*27*–*29*). The device uses a fluidic cell with a bottom surface micropatterned with circular pits, which are controllably sealed by pressing a convex lens against the planar top coverslip (fig. S2) (*30*). This permits the introduction of the kinesin motors and microtubules before the sealing of the chamber. The sealing prevents the landing of microtubules from solution occurring in open chambers and channels (*26*, *31*, *32*), which can confound the analysis. Initially, each chamber contains a total of 40 to 200 microtubules gliding at a velocity of 0.8 μm/s. The microtubules accumulate at the circular boundary within a minute after confinement and circle the chamber every 3 min, both clockwise and counterclockwise. Pinning events (*24*, *33*), where the tip of a gliding microtubule gets stuck (e.g., to a defective motor) as the motors propelling the tail buckle the microtubule (*34*), can redirect the microtubule away from the wall if it gets unstuck. These pinning events and the associated sharp turns (*35*, *36*) are partially responsible for the continued presence of microtubules away from the wall. Microtubules slowly release protofilament fragments from their leading end as they glide, which contributes to the free tubulin dimer concentration in solution that is conducive to microtubule growth and fusion events. Fusion events result from microtubules moving in the same direction and—because of velocity differences—catching up with each other. The leading minus end of one microtubule can then attach to a trailing plus end of the other microtubule by forming a partial connection between two protofilaments. After the initial attachment, free tubulin from the solution binds and fills the gaps in the connection (*37*) similar to the self-healing observed for microtubules (*38*, *39*). The closed chamber largely prevents ATP from entering; thus, the ATP concentration falls within hours because of motor activity, ultimately reducing microtubule gliding velocity and the frequency of collision events, bringing the assembly process to a stop (fig. S3 and movie S1).

Visual evidence that increasing length results from fusion and not polymerization is obtained by performing the experiment with a mixture of rhodamine- and HiLyte Fluor 647 (HiLyte)–labeled microtubules (Fig. 3A). Images taken 24 hours after the start of the experiment show long microtubules composed of segments with different colors, indicating that fusion events have occurred (Fig. 3, A and B, and Movie 2). Gaps and overlaps between gray and red microtubules occur because microtubules move in the time interval between the acquisition of the two fluorescence imaging channels (fig. S4). The initially 41 ± 1 microtubules per chamber (average ± SE, three chambers) form 20 ± 2 rhodamine-HiLyte Fluor connections after 24 hours (Fig. 3C). Although in some cases we can identify connections between segments of the same color (fig. S5), we count the always-identifiable rhodamine-HiLyte connections. The total number of connections is twofold higher, because the starting number of rhodamine and HiLyte microtubules is similar. The number of microtubules is reduced because of fusion and depolymerization of short microtubules and can increase because of microtubule breaking, leading to 10 ± 2 microtubules per chamber after 24 hours. The distribution of the number of connections per microtubule after 24 hours is consistent with the exponential distribution of a step growth polymerization process (Fig. 3D and fig. S6) (*40*).

Microtubule fusion is accelerated 20-fold by the confinement in the chamber

The acceleration of the fusion process by the circular boundary is demonstrated by a comparison between fusion in the circular chamber and fusion on a planar surface, where a similar initial number of microtubules per surface area leads only very rarely to a fusion event (Fig. 4A). For a similar initial surface density (86 microtubules per chamber and 75 microtubules in an equal area without

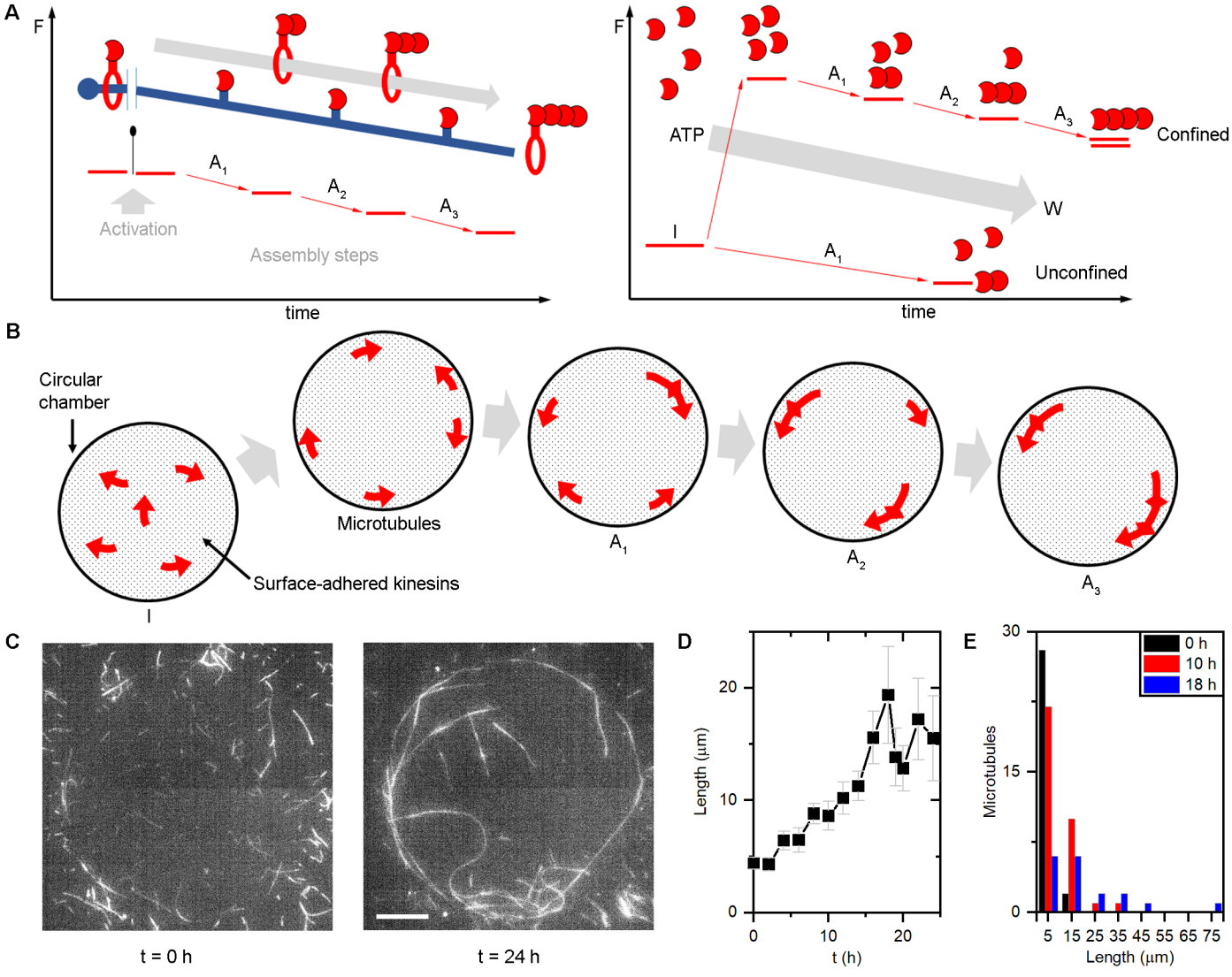

Fig. 2. Motor-driven molecular assembly. (**A**) Previous molecular robots/machines [sketched is the catalytic machine of De Bo *et al.* (*6*)] often rely on entropically driven movement where the free energy *F* of the mover decreases over time, whereas molecular motors can use fuel, such as ATP, to enable assembly steps. Confinement of motion generates a distribution of building blocks with higher free energy *F* and can accelerate assembly. (**B**) This principle is realized in a system where microtubules are propelled by surface-adhered, ATP-consuming kinesin-1 motor proteins in a circular chamber (diameter, 50 μm; height, 0.5 μm) where end-to-end fusion of microtubules can occur. (**C**) Fluorescence microscopy images of rhodamine-labeled microtubules at 0 and 24 hours after confinement. Scale bar, 10 μm. (**D**) Average microtubule length as a function of time. There are 56 microtubules in the chamber at $t = 0$ hours. The error bars show the SE ($34 \geq n \geq 14$). (**E**) Histogram of the microtubule lengths at 0 (black), 10 (red), and 18 (blue) hours. The bin width is 10 μm, and the labels indicate the middle of the bin.

confinement), 60 rhodamine-HiLyte connections are formed in the chamber in 10 hours versus only 3 connections on an equal area of the planar surface (Fig. 4B and fig. S7). The notable difference in the fusion rate is underscored by the evolution of the microtubule number (Fig. 4C), which declines as a result of fusion in the chamber but is constant on the planar surface. The number of microtubules is also affected by depolymerization of short microtubules, breaking of microtubules, and—in the unconfined case—landing and leaving microtubules (*35*, *41*). The initial bimolecular reaction rate is 0.1 day^{-1} for the confined and 0.001 day^{-1} for the unconfined case (concentrations expressed in number of microtubules per chamber area, yielding reaction rates in number of fusion events per chamber area and time; see the "Calculating the bimolecular reaction rate" section in the Supplementary Materials). Both the gliding velocity of the microtubules and the fraction of moving microtubules decrease over the course of the experiment (Fig. 4D), although the effect is more pronounced in the circular chamber because of restricted access to ATP.

The role of the gliding velocity in the fusion process is complex, because the frequency of plus-end to minus-end collisions between two microtubules circling the chamber is proportional to their velocity difference, while the time available to successfully fuse is inversely proportional to the velocity difference. The resulting dependence of the fusion process on the gliding velocity distribution may be nonmonotonic, as has been observed for the velocity-dependent process of gliding microtubules picking up cargo from

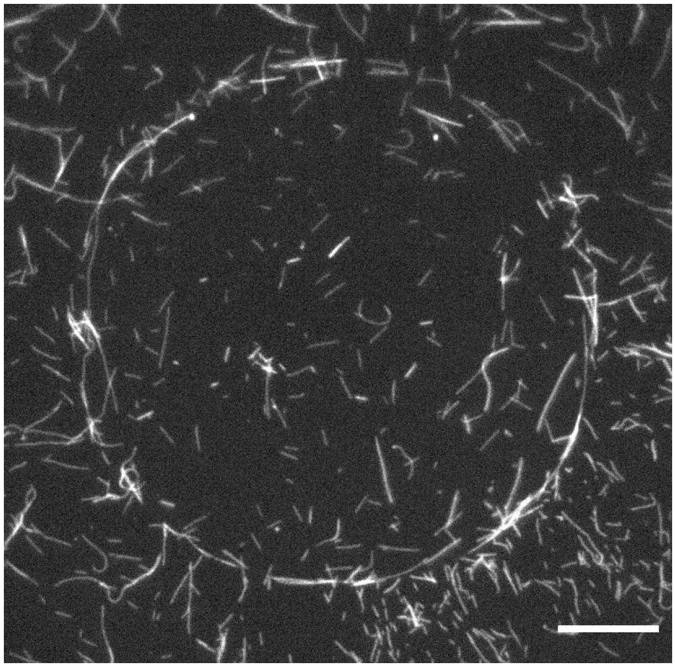

Movie 1. Kinesin-propelled rhodamine-labeled microtubules confined in a chamber, imaged immediately after confinement. Time accelerated by a factor of 50. Scale bar, 10 μm.

the surface (*42*). In our experiments, both microtubule density and velocity drop over time (fig. S8A), and the mean absolute velocity difference decreases with the decreasing velocity (fig. S8B). The fusion rate increases with the number of moving microtubules but does not show a clear dependence on the velocity or velocity difference (fig. S8C).

The confinement induces a nonequilibrium microtubule distribution

Microtubule fusion is accelerated by the nonequilibrium state achieved by the work of kinesins propelling the microtubules. To assess the minimum energy required to achieve this high-energy state, we calculate the change in free energy between the initial and nonequilibrium states. This free energy change is composed of the energy expenditures required to move the initially randomly distributed and oriented microtubules to the wall (decreasing entropy), align them with the wall (decreasing entropy), and bend them into the curvature of the wall (increasing internal energy). The elastic bending energy stored in 3-μm-long microtubules with a persistence length of 50 μm (fig. S9) after the boundary with curvature 1/25 μm^{-1} is 0.1 k_BT (where k_B is the Boltzmann constant and T is temperature). In our experiment, the resolution of the fluorescence microscope limits the precision with which the positional and angular distributions can be determined (Fig. 5, A and B). By modeling the bounded persistent random walk of the gliding microtubules with a persistence length of 50 μm, we obtained simulated steady-state

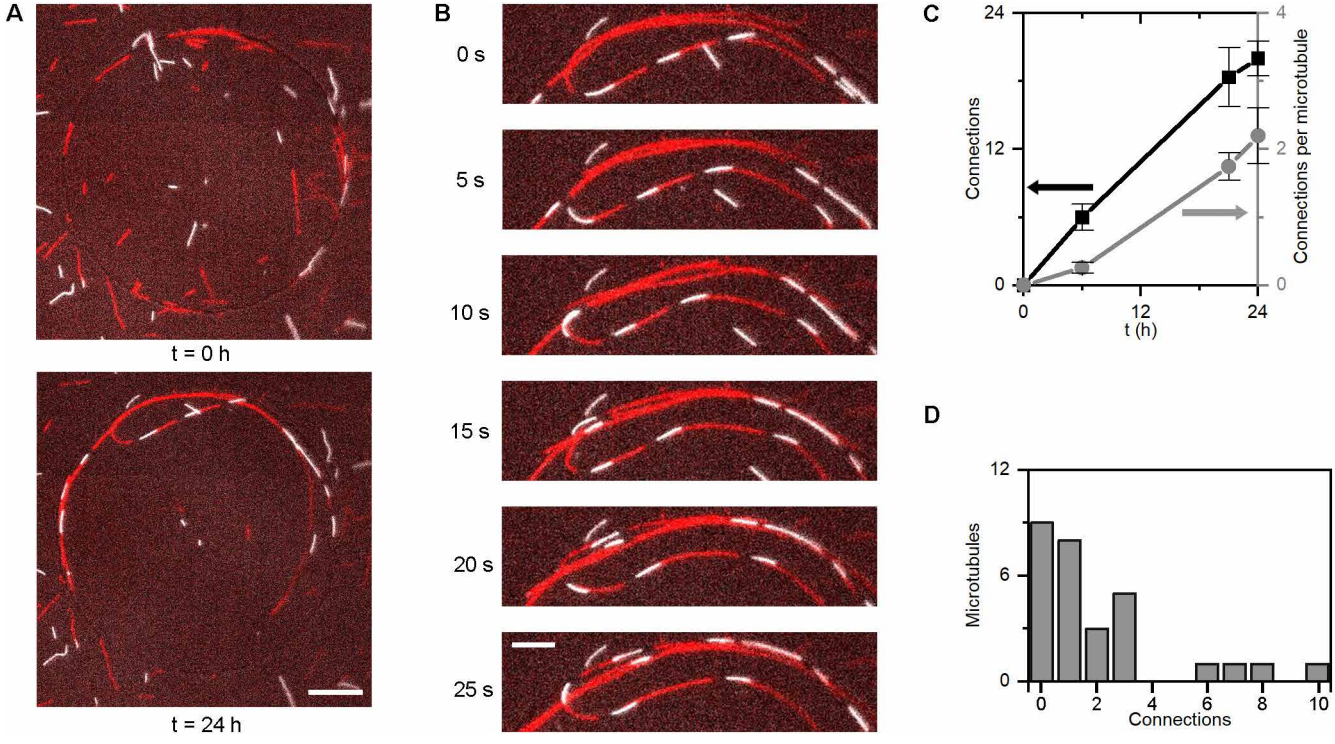

Fig. 3. Fusion of microtubules with different fluorescent labels. (**A**) Overlaid fluorescence microscopy images of kinesin-propelled rhodamine (gray)– and HiLyte (red)–labeled microtubules confined in a 50-μm chamber at the start of the experiment and after 24 hours. Scale bar, 10 μm. (**B**) Time-lapse images of a region of interest taken after 24 hours at intervals of 5 s. Scale bar, 5 μm. (**C**) The number of rhodamine-HiLyte connections between microtubules (black) and the average number of rhodamine-HiLyte connections per microtubule (gray) as a function of time for the experiment shown in (A) and (B). Mean of three chambers, SE. (**D**) Histogram of the number of rhodamine-HiLyte connections per microtubule after 24 hours (29 microtubules pooled from three chambers).

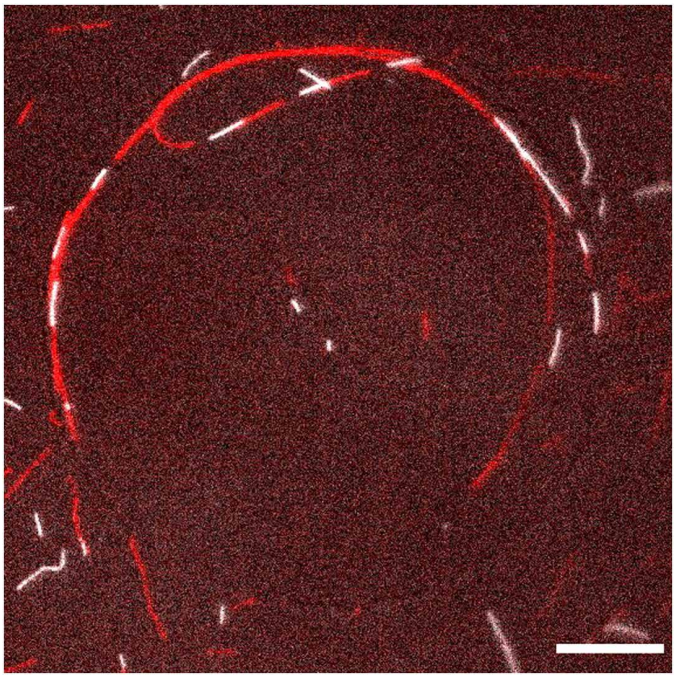

Movie 2. Kinesin-propelled rhodamine (gray)– and HiLyte (red)–labeled microtubules confined in a chamber, imaged 24 hours after confinement. Time accelerated by a factor of 50. Scale bar, 10 μm.

distributions for the microtubule density and orientation relative to the boundary (Fig. 5C, "Simulation of microtubules as active Brownian particles" section in the Supplementary Materials, and fig. S10) (*43*), similar to the earlier analysis of Månsson *et al.* (*26*). Our simulations (Fig. 5C), which match the experimental observations (Fig. 5, A and B) well, show that the entropy change due to the concentration and alignment of each tip is $-2\ k_B$ ("Radial and angular distribution entropy calculation" section in the Supplementary Materials and fig. S11). The minimal work per microtubule required to create the nonequilibrium distribution of microtubules near the circular boundary by increasing their internal energy and reducing their translational and rotational entropy is therefore 2 to 3 k_BT.

The work done by the motors to reduce the range of microtubule directions and positions results in an increased frequency of end-to-end collisions under suitable angles and thereby accelerates the fusion process, just as the isothermal compression of reactive gas molecules in a cylinder increases their reaction rate. For an ideal gas, doubling the rate of collisions by isothermal compression requires $k_BT\ln 2$ of work per particle (*44*). Similarly, the roughly 2^4-fold acceleration achieved in the experiment shown in Fig. 4 was achieved by doing work in the amount of 3 k_BT (= 4 $k_BT\ln 2$) per microtubule to compress the accessible phase space of positions and angles.

During the process of alignment with the boundary, the microtubule transitions over an energy barrier, because the gliding microtubule turns sharply as the boundary is reached and then follows the boundary in either a clockwise or counterclockwise direction (Fig. 5, D and E). The sharp turn with a radius of curvature of 1 μm

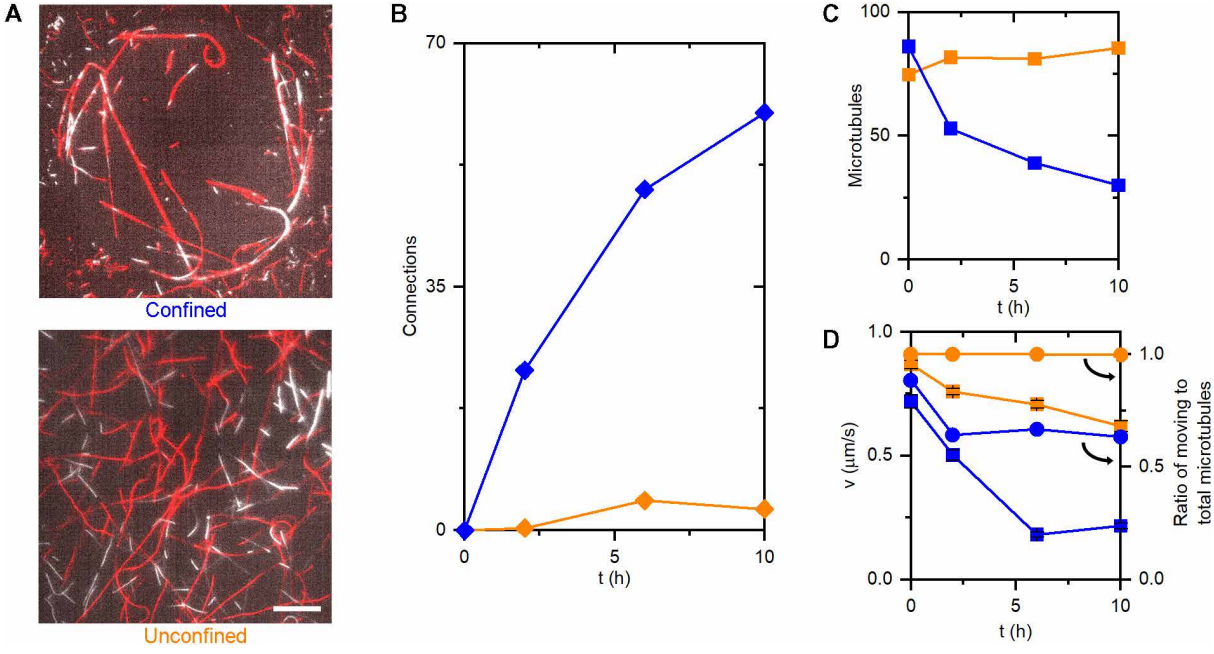

Fig. 4. Movement along the wall increases microtubule fusing. (**A**) Fluorescence microscopy images of kinesin-propelled rhodamine (gray)– and HiLyte (red)– labeled microtubules confined in a chamber and moving without constraint on the surface after 24 hours. Scale bar, 10 μm. (**B**) The number of rhodamine-HiLyte connections as a function of time for microtubules confined in a chamber (blue) and unconfined on an equal surface area (orange). (**C**) The number of microtubules as a function of time for confined (blue) and unconfined (orange) microtubules. (**D**) The velocity of moving microtubules (squares) and the ratio of moving microtubules to total microtubules (circle) for confined (blue) and unconfined (orange) microtubules. Error bars for the velocity represent the SE ($n > 10$) and are smaller than the symbols.

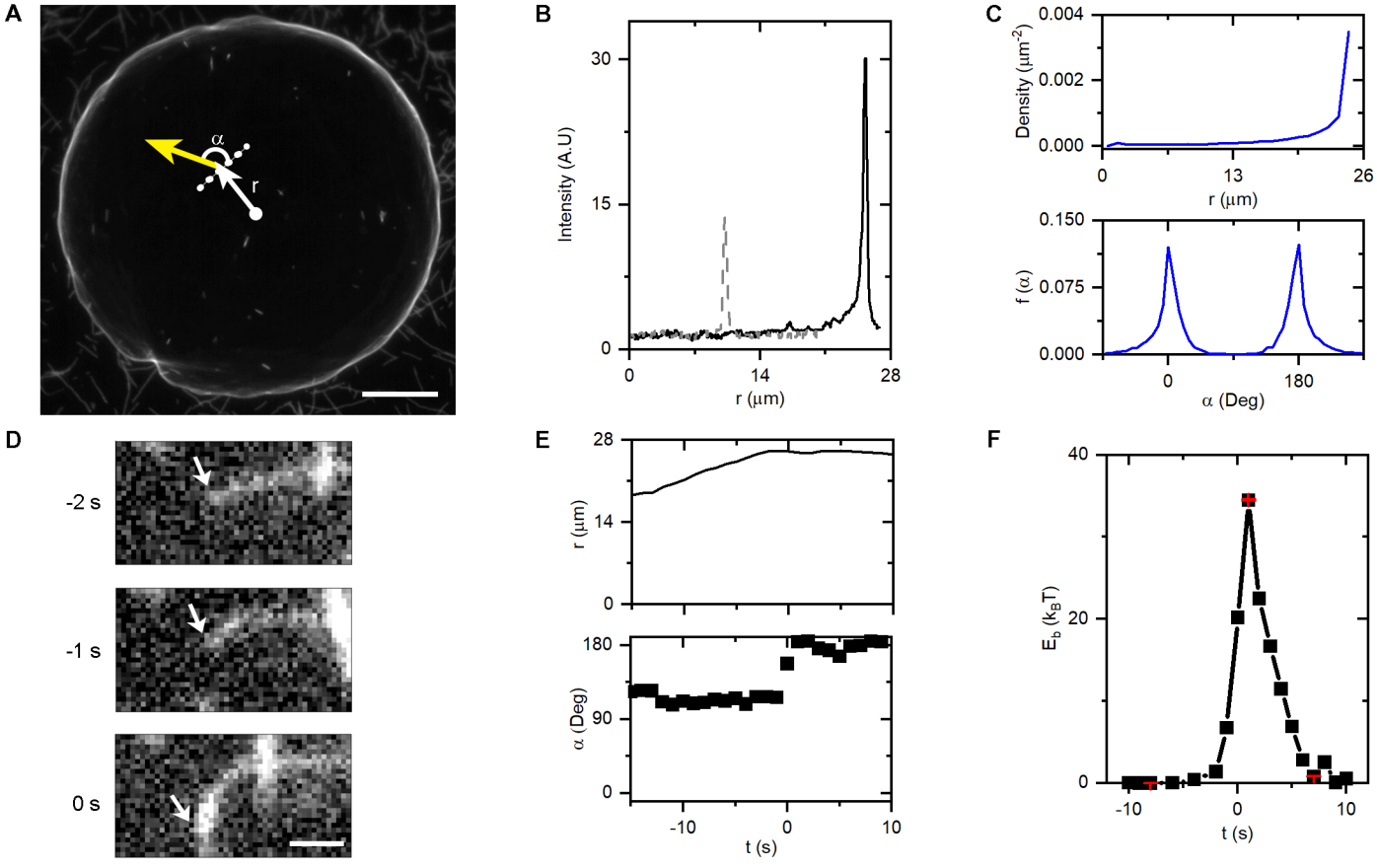

Fig. 5. Gliding microtubules collide with the boundary and align with it in an energy-consuming process, leading to the emergence of a nonequilibrium radial and angular distributions. (**A**) Median intensity of 301 fluorescent microscopy images of 180 rhodamine-labeled microtubules in a chamber taken 0 hours after confinement every 1 s. Scale bar, 10 μm. Each microtubule can be described by the radial (*r*) and angular position of its tip and the angle of its movement relative to the boundary (α). (**B**) Relative intensity as a function of distance from the center of the chamber for two 1-μm-wide sections of the image in (A), one with (dashed gray line) and one without (solid black line) a stuck microtubule crossing the radius. A.U., arbitrary units. (**C**) Brownian dynamics simulations of the persistent random walk yield the theoretical density and angle distributions (see also fig. S11) of microtubules gliding under confinement. (**D**) Fluorescence microscopy images of a microtubule as it encounters and aligns with the wall. The white arrow marks the tip of the microtubule. Scale bar, 1 μm. (**E**) The radial position, *r*, and the angle relative to the boundary, α, of the microtubule shown in (D) over time. To reduce the impact of localization noise, the angle is determined from the tip position at time *t* and time *t* − 3 s. (**F**) The bending energy $E_b = k_B T L_p \Sigma \kappa_i^2 L_i/2$ of the microtubule in units of $k_B T$ as a function of time for the microtubule shown in (D) and (E) calculated from the curvatures κ_i of $L_i \approx 0.5$-μm-long segments and persistence length $L_p = 50$ μm. The red error bars at $t = -8$, 1, and 7 s represent the SD of three tracings of the microtubule and are smaller than the symbols.

increases the elastic energy stored in the microtubule to close to 40 k_BT during the initial alignment (Fig. 5F), although the subsequent rupture of kinesin-microtubule attachments allows for an increased curvature and relaxes the elastic strain on the microtubule (Fig. 5F), as previously predicted by simulations of alignment processes (*45*). This bending energy is almost completely dissipated after the microtubule exits the sharp turn, contributing to the frictional losses in the transition from the initial distribution of the microtubules to the steady-state distribution with the microtubules following the wall.

DISCUSSION

The experiments demonstrate that the interaction of motor-driven active transport and confinement leads to a region of high microtubule density, where the rate of end-to-end fusion of microtubules is more than 10-fold accelerated. The simulations show that the compression of the microtubule phase space defined by location and orientation requires work of 3 $k_B T$; although during the alignment with the wall, the elastic energy stored in the microtubule transiently reaches close to 40 $k_B T$.

However, the chemical energy expended during the fusion process is dominated by the ATP consumption of the dozens of kinesin motors propelling each microtubule. For the experiment shown in Fig. 4, 86 microtubule segments with a length of 3 μm are propelled by kinesins with a linear density of 20 μm^{-1} each consuming 90 ATP molecules per second over 10 hours, which yields a fuel expenditure per connection on the order of 100 million ATP molecules, each with an energy content of 20 k_BT (calculated for the ATP, adenosine diphosphate, and inorganic phosphate concentrations of 2.5 mM present at the midpoint of the ATP utilization), for a total of 10 pJ. The energy required for the mechanical bending of the

microtubule, which is the source of the nonequilibrium distribution accelerating the reaction, is thus dwarfed by the energy expended to actively move the microtubules. To a large degree, this is due to the more than million-fold mismatch between the low viscous drag required to move the microtubule and the large potential force produced by the many kinesin motors. However, other nanoscale propulsion mechanisms, such as self-electrophoretic and bubble-powered catalytic micromotors, have even lower efficiencies (*46*). The lower limit for the energy expenditure per connection can be approached by increasing the efficiency of the transport (e.g., by reducing the motor density). What must remain (even if a negligible amount of energy is dissipated during transport) is the change in the internal energy and translational and rotational entropy calculated previously (2 to 3 k_BT).

Whereas many chemical reactors operate near their thermodynamic limits (*47*), computers have had commercial success while operating far from their thermodynamic limits (*48*), although the minimal energy dissipation depends on the rate of computation (*49*). Macroscopic robots are similar to our system in that they expend most energy on overcoming friction and potential energy barriers. Although the discussion of efficiency frequently focuses on the efficiency of the motor (*50*), here, the focus is on the efficiency of the utilization of the force produced by molecular motors (*51*). Clearly, both force generation and utilization have to be performed with high efficiency to compete with molecular and nanoscale assembly processes enabled by thermal forces. Our main points are that a thermodynamic lower limit for the energy expenditure for a given acceleration of assembly exists (*44*) and that our process operates far from this limit although it relies on highly efficient biomolecular motors.

The question of whether such a nanoscale system meets the definition of a robot (*52*) has been previously answered in the affirmative by Lund *et al.* (*11*), who constructed a similar system consisting of a DNA walker showing elementary robotic behavior as it is guided by its environment. Our system also carries out a complex series of actions automatically (*53*), consisting of the microtubules finding the boundary, reorienting, following the boundary, and selectively fusing with other, suitably positioned microtubules. All these actions can be considered to be "embedded," seemingly requiring neither sensing nor computing, merely actuation. "Intelligence"—however limited—is thus provided by the designer rather than the system (*54*), although in the context of the engineering of bipedal robots, the exploitation of passive dynamics was considered a major breakthrough (*55*). From a different perspective, the molecular robot explores its environment via thermal shape fluctuations or reversible reactions, senses the local potential energy landscape, selects a path close to the minimum energy path, and proceeds along this path via irreversible dissipation of energy. A branching of the available paths forces a decision (*56*) and can activate a new sequence of actions. For example, in our system, the microtubule tip experiences thermal fluctuations, interacts with the wall, spends most of its time close to the angular position where the wall-imposed bending is minimized, and is propelled forward along a particular angular direction by the ATP-consuming and effectively irreversible action of the kinesin motors. A new "subroutine" is executed if the microtubule tip encounters the tail of another microtubule, tubulin-tubulin interactions stabilize the aligned configuration, and free tubulin dimers are recruited from solution to fuse the microtubules. From the perspective of the chemist, these processes are merely the result of the dynamics of a molecular system on a particularly large and complex energy landscape. From the perspective of a biologist, these processes recapitulate the exploration of a maze by a rat using its whiskers or by a fungus using its hypha (*57*), that is, sequences of sensing, computation, and actuation that are ultimately resulting from molecular events as well. For the roboticist, this in vitro system is recognizable as a robot, because its systems parameters can be engineered. For example, microtubule rigidity can be predictably altered to tune the parameters of the microtubule tip's sensing function, the motor surface density will affect force production, and microtubule interactions can be specified with different linkers. These programmable interactions allow for swarm behavior (*17*) although not yet at the level of functionality of macroscopic robot swarms (*58*, *59*). Algorithms for the control and programming of molecular and nanoscale robots are an active area of research (*10*, *60*).

A practical example of how the generation of a nonequilibrium distribution can be beneficial is the label-free biosensor demonstrated by Chaudhuri *et al.* (*61*), which relies on the detection of the aggregation of kinesin-propelled microtubules in response to the capture of the analyte by the microtubules. The microtubule aggregation step and thereby the time required for analyte detection could be accelerated by using a guiding structure (*62*). However, the end-to-end fusion assembly process studied here provides a clearer demonstration of the effect, because it takes advantage of both the increased density and the higher degree of alignment of the microtubules.

A common feature of the previously demonstrated molecular machines and robots for active chemical assembly (*3*, *5*–*9*, *14*, *63*, *64*) is that the molecular machine/robot and its support (e.g., the DNA origami tile) are initially in a "charged," high-energy state and relax under the effect of an enthalpic or entropic driving force in complex series of orchestrated steps toward the equilibrium state. For example, the rotaxane used by De Bo *et al.* (*6*) to synthesize a polymer chain is initially constrained to a specific position and diffusively explores the increasing space made available by the progressing assembly process. The charging is accomplished in the course of a suitable assembly sequence for the initial structure.

An interesting aspect of the system described here is that the system "charges itself" as the microtubules starting from random positions in the circular chamber are propelled toward a nonequilibrium distribution near the chamber wall by the action of the motors. This is also different from the widely studied assembly of cytoskeletal filaments propelled by surface-adhered motor proteins into larger structures, such as spools (*65*) and bundles (*17*, *61*), where motor-driven active transport enables and accelerates the formation of energetically unfavorable assemblies.

The contribution of our work and other related studies is best appreciated in the context of current bioinspired efforts to design molecular factories, where multistep chemical transformations such as the biocatalytic assembly of HIV drugs (*66*) are designed to take place in one or more compartments (*67*). Although the state of the art is the engineering of smooth flows from building blocks to products driven by the free energy changes of the reaction steps (*68*), further improvements become possible through the integration of molecular robots capable of accelerating the flow and assembly of molecular parts.

Although our system highlights the large gap between energetic limits for the acceleration of molecular self-assembly processes, and

the large frictional losses present in molecular motor-driven transport, it also points toward a future where molecular machines do work to access nonequilibrium states and exponentially accelerate molecular and nanoscale assembly.

MATERIALS AND METHODS

Microtubule preparation

Microtubules were polymerized from 20 μg of lyophilized rhodamine (Cytoskeleton Inc., TL590M) or HiLyte Fluor 647 (Cytoskeleton Inc., TL670M)–labeled tubulin in 6.25 μl of polymerization buffer [BRB80 buffer, with 4 mM $MgCl_2$, 1 mM guanosine triphosphate (GTP), and 5% dimethylsulfoxide]. BRB80 buffer is composed of 80 mM piperazine-*N*,*N*′-bis (2-ethanesulphonic acid), 1 mM $MgCl_2$, and 1 mM EGTA, adjusted to a pH of 6.89 with potassium hydroxide. The solution was incubated on ice for 5 min and placed into a 37°C water bath for 45 min. The solution was then diluted 20-fold to a concentration of 0.15 mg/ml of tubulin into BRB80 buffer containing 50 μM paclitaxel.

Kinesin preparation

Kinesin was prepared by the team of G. Bachand at the Center for Integrated Nanotechnologies (Sandia National Laboratory). Wild-type, full-length *Drosophila melanogaster* kinesin heavy chain with a C-terminal His tag (*69*) was expressed in *Escherichia coli*, purified using a Ni–nitrilotriacetic acid column, and flash-frozen with liquid nitrogen in kinesin buffer [40 mM imidazole, 300 mM NaCl, EGTA (0.76 g/liter), EDTA (37 mg/liter), sucrose (50 g/liter), 0.2 mM TCEP (tris(2-carboxyethyl)phosphine) and 50 μM Mg-ATP at pH 7].

Gliding assay

Flow cells (25 mm by 25 mm) were fabricated and assembled by ScopeSys Inc. The flow cells were composed of two thin coverslips sandwiched together with 30-μm double-sided adhesive tape (Nitto Corp., no. 5603). For the confinement measurements, the bottom coverslip has embedded wells 50 to 55 μm in diameter and 500 nm deep, whereas for the control experiments, the coverslip did not have the wells. The flow cell was loaded with BRB80 buffer containing casein (6 mg/ml). After 10 min, the solution was exchanged with the kinesin motor solution [BRB80 buffer with casein (4 mg/ml), 5 mM ATP, and kinesin fivefold diluted from the stock solution], which was exchanged, 10 min later, against a microtubule solution containing tubulin (0.02 or 0.01 mg/ml) in the Motility Solution buffer [casein (0.5 mg/ml), 10 μM paclitaxel, 5 mM ATP, 20 mM D-glucose, glucose oxidase (0.2 mg/ml), catalase (8 μg/ml), and 10 mM dithiothreitol in BRB80]. For some measurements, the microtubules used were all rhodamine-labeled microtubules, and for some, we used a mixture of half rhodamine-labeled and half HiLyte-labeled microtubules. The GTP concentration was 1 to 5 μM in the experiments based on the dilution of the polymerization solution. For the experiments of microtubules confined in a chamber, the CLiC rod-lens was placed on the top coverslip above a well and lowered to push down the top coverslip, creating a closed chamber (fig. S2) as previously demonstrated (*28*). Adjacent wells were also sealed and could be imaged by moving the stage. All experiments were performed at 24° ± 2°C. We analyzed more than 10 independent experiments; for most of them, one chamber was imaged and analyzed, whereas for some, three or four chambers were imaged and analyzed.

Microscopy

The gliding assay was imaged using a Nikon Eclipse Ti epifluorescence microscope equipped with a scientific Complementary metal–oxide–semiconductor camera (Zyla 4.2, Andor Inc.), a "perfect focus" system to keep the surface in focus over days, and a 100× oil objective [numerical aperture (NA) = 1.49] or 40× oil objective (NA = 1.3). The sample was illuminated with a 488-nm laser (Omicron-Laserage Laserprodukte) operating at nominally 8% of the 150-mW maximal power or a light-emitting diode–based white light source (SOLA light engine, Lumencor Inc.) operating at 8% of the maximal power for the rhodamine-labeled microtubules and a 647-nm laser (Omicron-Laserage Laserprodukte) operating at 5% of the 140-mW maximal power for the HiLyte-labeled microtubules. The excitation light was on only during the camera exposure time window. For the exposures with the laser light, we used total internal reflection fluorescence illumination. The camera exposure time was 50 ms when the SOLA was used and 30 ms when the lasers were used.

Analysis

The images were analyzed using Fiji ImageJ software and MATLAB (MathWorks Inc.). The number of moving, stuck, and total microtubules was counted for all the microtubules in the chamber or for all microtubules in the field of view and normalized to the equivalent chamber area in the unconfined measurements. The length was measured using the ImageJ Segmented Line function for all the microtubules in the chamber or at least 14 microtubules in the chamber chosen randomly. The number of connections was measured for all microtubules in the chamber or in the unconfined measurements for all microtubules in the field of view and normalized to the equivalent chamber area. Microtubule locations and velocities were measured with the Manual Tracking plugin in ImageJ, and MATLAB was used to calculate the average velocity, velocity mean difference, angles, distance from center, and persistence length. The median intensity was measured using Z Project in ImageJ. For the bending energy, a spline was fit to the data in MATLAB using CVX, a package for specifying and solving convex programs (*70*, *71*).

Simulations

The simulations were performed and analyzed in MATLAB (MathWorks Inc.) and detailed in the Supplementary Materials.

SUPPLEMENTARY MATERIALS

www.science.org/doi/10.1126/scirobotics.abj7200
Calculating the bimolecular reaction rate
Simulation of microtubules as active Brownian particles
Radial and angular distribution entropy calculation
Figs. S1 to S11
Movie S1

REFERENCES AND NOTES

1. C. Pezzato, C. Cheng, J. F. Stoddart, R. D. Astumian, Mastering the non-equilibrium assembly and operation of molecular machines. *Chem. Soc. Rev.* **46**, 5491–5507 (2017).
2. K. E. Drexler, Molecular engineering - an approach to the development of general capabilities for molecular manipulation. *Proc. Natl. Acad. Sci.* **78**, 5275–5278 (1981).
3. P. Thordarson, E. J. A. Bijsterveld, A. E. Rowan, R. J. M. Nolte, Epoxidation of polybutadiene by a topologically linked catalyst. *Nature* **424**, 915–918 (2003).
4. C. Monnereau, P. H. Ramos, A. B. C. Deutman, J. A. A. W. Elemans, R. J. M. Nolte, A. E. Rowan, Porphyrin macrocyclic catalysts for the processive oxidation of polymer substrates. *J. Am. Chem. Soc.* **132**, 1529–1531 (2010).
5. B. Lewandowski, G. De Bo, J. W. Ward, M. Papmeyer, S. Kuschel, M. J. Aldegunde, P. M. E. Gramlich, D. Heckmann, S. M. Goldup, D. M. D'Souza, A. E. Fernandes, D. A. Leigh,

Sequence-specific peptide synthesis by an artificial small-molecule machine. *Science* **339**, 189–193 (2013).
6. G. De Bo, M. A. Y. Gall, S. Kuschel, J. De Winter, P. Gerbaux, D. A. Leigh, An artificial molecular machine that builds an asymmetric catalyst. *Nat. Nanotechnol.* **13**, 381–385 (2018).
7. S. Kassem, A. T. L. Lee, D. A. Leigh, V. Marcos, L. I. Palmer, S. Pisano, Stereodivergent synthesis with a programmable molecular machine. *Nature* **549**, 374–378 (2017).
8. W. Meng, R. A. Muscat, M. L. McKee, P. J. Milnes, A. H. El-Sagheer, J. Bath, B. G. Davis, T. Brown, R. K. O'Reilly, A. J. Turberfield, An autonomous molecular assembler for programmable chemical synthesis. *Nat. Chem.* **8**, 542–548 (2016).
9. J. Jin, E. G. Baker, C. W. Wood, J. Bath, D. N. Woolfson, A. J. Turberfield, Peptide assembly directed and quantified using megadalton DNA nanostructures. *ACS Nano* **13**, 9927–9935 (2019).
10. A. J. Thubagere, W. Li, R. F. Johnson, Z. Chen, S. Doroudi, Y. L. Lee, G. Izatt, S. Wittman, N. Srinivas, D. Woods, E. Winfree, L. Qian, A cargo-sorting DNA robot. *Science* **357**, eaan6558 (2017).
11. K. Lund, A. J. Manzo, N. Dabby, N. Michelotti, A. Johnson-Buck, J. Nangreave, S. Taylor, R. J. Pei, M. N. Stojanovic, N. G. Walter, E. Winfree, H. Yan, Molecular robots guided by prescriptive landscapes. *Nature* **465**, 206–210 (2010).
12. J. Chao, J. Wang, F. Wang, X. Ouyang, E. Kopperger, H. Liu, Q. Li, J. Shi, L. Wang, J. Hu, L. Wang, W. Huang, F. C. Simmel, C. Fan, Solving mazes with single-molecule DNA navigators. *Nat. Mater.* **18**, 273–279 (2019).
13. A. Bazrafshan, T. A. Meyer, H. Su, J. M. Brockman, A. T. Blanchard, S. Piranej, Y. Duan, Y. Ke, K. Salaita, Tunable DNA origami motors translocate ballistically over μm distances at nm/s speeds. *Angew. Chem. Int. Ed.* **59**, 9514–9521 (2020).
14. F. J. Nedelec, T. Surrey, A. C. Maggs, S. Leibler, Self-organization of microtubules and motors. *Nature* **389**, 305–308 (1997).
15. O. Idan, A. Lam, J. Kamcev, J. Gonzales, A. Agarwal, H. Hess, Nanoscale transport enables active self-assembly of millimeter-scale wires. *Nano Lett.* **12**, 240–245 (2012).
16. T. Sanchez, D. T. N. Chen, S. J. DeCamp, M. Heymann, Z. Dogic, Spontaneous motion in hierarchically assembled active matter. *Nature* **491**, 431–434 (2012).
17. J. J. Keya, R. Suzuki, A. M. R. Kabir, D. Inoue, H. Asanuma, K. Sada, H. Hess, A. Kuzuya, A. Kakugo, DNA-assisted swarm control in a biomolecular motor system. *Nat. Commun.* **9**, 453 (2018).
18. G.-Z. Yang, J. Bellingham, P. E. Dupont, P. Fischer, L. Floridi, R. Full, N. Jacobstein, V. Kumar, M. M. Nutt, R. Merrifield, B. J. Nelson, B. Scassellati, M. Taddeo, R. Taylor, M. Veloso, Z. L. Wang, R. Wood, The grand challenges of Science Robotics. *Sci. Robot.* **3**, eaar7650 (2018).
19. L. Ricotti, B. Trimmer, A. W. Feinberg, R. Raman, K. K. Parker, R. Bashir, M. Sitti, S. Martel, P. Dario, A. Menciassi, Biohybrid actuators for robotics: A review of devices actuated by living cells. *Sci. Robot.* **2**, eaaq0495 (2017).
20. S. W. Rothwell, W. A. Grasser, D. B. Murphy, End-to-end annealing of microtubules in vitro. *J. Cell Biol.* **102**, 619–627 (1986).
21. M. Caplow, J. Shanks, B. P. Brylawski, Differentiation between dynamic instability and end-to-end annealing models for length changes of steady-state microtubules. *J. Biol. Chem.* **261**, 16233–16240 (1986).
22. Y. Jeune-Smith, H. Hess, Engineering the length distribution of microtubules polymerized in vitro. *Soft Matter* **6**, 1778–1784 (2010).
23. N. F. Bouxsein, G. D. Bachand, Single filament behavior of microtubules in the presence of added divalent counterions. *Biomacromolecules* **15**, 3696–3705 (2014).
24. T. Nitta, H. Hess, Dispersion in active transport by kinesin-powered molecular shuttles. *Nano Lett.* **5**, 1337–1342 (2005).
25. N. Isozaki, H. Shintaku, H. Kotera, T. L. Hawkins, J. L. Ross, R. Yokokawa, Control of molecular shuttles by designing electrical and mechanical properties of microtubules. *Sci. Robot.* **2**, eaan4882 (2017).
26. A. Månsson, R. Bunk, M. Sundberg, L. Montelius, Self-organization of motor-propelled cytoskeletal filaments at topographically defined borders. *J. Biomed. Biotechnol.* **2012**, 647265 (2012).
27. S. R. Leslie, A. P. Fields, A. E. Cohen, Convex lens-induced confinement for imaging single molecules. *Anal. Chem.* **82**, 6224–6229 (2010).
28. D. J. Berard, M. Shayegan, F. Michaud, G. Henkin, S. Scott, S. Leslie, Formatting and ligating biopolymers using adjustable nanoconfinement. *Appl. Phys. Lett.* **109**, 033702 (2016).
29. N. K. Thiombane, N. Coutin, D. Berard, R. Tahvildari, S. Leslie, C. Nislow, Single-cell analysis for drug development using convex lens-induced confinement imaging. *BioTechniques* **67**, 210–217 (2019).
30. M. J. Ahamed, S. Mahshid, D. J. Berard, F. Michaud, R. Sladek, W. W. Reisner, S. R. Leslie, Continuous confinement fluidics: Getting lots of molecules into small spaces with high fidelity. *Macromolecules* **49**, 2853–2859 (2016).
31. Y. Hiratsuka, T. Tada, K. Oiwa, T. Kanayama, T. Q. P. Uyeda, Controlling the direction of kinesin-driven microtubule movements along microlithographic tracks. *Biophys. J.* **81**, 1555–1561 (2001).
32. M. G. van den Heuvel, C. T. Butcher, R. M. Smeets, S. Diez, C. Dekker, High rectifying efficiencies of microtubule motility on kinesin-coated gold nanostructures. *Nano Lett.* **5**, 1117–1122 (2005).
33. D. G. Weiss, G. M. Langford, D. Seitz-Tutter, W. Maile, Analysis of the gliding, fishtailing and circling motions of native microtubules. *Acta Histochem. Suppl.* **41**, 81–105 (1991).
34. I. Luria, J. Crenshaw, M. Downs, A. Agarwal, S. B. Seshadri, J. Gonzales, O. Idan, J. Kamcev, P. Katira, S. Pandey, T. Nitta, S. R. Phillpot, H. Hess, Microtubule nanospool formation by active self-assembly is not initiated by thermal activation. *Soft Matter* **7**, 3108–3115 (2011).
35. E. L. P. Dumont, C. Do, H. Hess, Molecular wear of microtubules propelled by surface-adhered kinesins. *Nat. Nanotechnol.* **10**, 166–169 (2015).
36. J. J. Keya, D. Inoue, Y. Suzuki, T. Kozai, D. Ishikuro, N. Kodera, T. Uchihashi, A. M. R. Kabir, M. Endo, K. Sada, A. Kakugo, High-resolution imaging of a single gliding protofilament of tubulins by HS-AFM. *Sci. Rep.* **7**, 6166 (2017).
37. M. Bachand, N. F. Bouxsein, S. Cheng, S. J. von Hoyningen-Huene, M. J. Stevens, G. D. Bachand, Directed self-assembly of 1D microtubule nano-arrays. *RSC Adv.* **4**, 54641–54649 (2014).
38. L. Schaedel, K. John, J. Gaillard, M. V. Nachury, L. Blanchoin, M. Thery, Microtubules self-repair in response to mechanical stress. *Nat. Mater.* **14**, 1156–1163 (2015).
39. S. Triclin, D. Inoue, J. Gaillard, Z. M. Htet, M. E. DeSantis, D. Portran, E. Derivery, C. Aumeier, L. Schaedel, K. John, C. Leterrier, S. L. Reck-Peterson, L. Blanchoin, M. Théry, Self-repair protects microtubules from destruction by molecular motors. *Nat. Mater.* **20**, 883–891 (2021).
40. P. J. Flory in *Principles of Polymer Chemistry* (Cornell Univ. Press, 1990), pp. 321–322.
41. N. M. Bassir Kazeruni, J. Rodriguez, G. Saper, H. Hess, Microtubule detachment in gliding motility assays limits the performance of kinesin-driven molecular shuttles. *Langmuir* **36**, 7901–7907 (2020).
42. A. Agarwal, P. Katira, H. Hess, Millisecond curing time of a molecular adhesive causes velocity-dependent cargo-loading of molecular shuttles. *Nano Lett.* **9**, 1170–1175 (2009).
43. T. Nitta, H. Hess, Effect of path persistence length of molecular shuttles on two-stage analyte capture in biosensors. *Cell. Mol. Bioeng.* **6**, 109–115 (2013).
44. H. Hess, A Landauer limit for robotic manipulation. arXiv:1803.07415 [cond-mat.stat-mech] (16 March 2018).
45. Y. Ishigure, T. Nitta, Understanding the guiding of kinesin/microtubule-based microtransporters in microfabricated tracks. *Langmuir* **30**, 12089–12096 (2014).
46. W. Wang, T.-Y. Chiang, D. Velegol, T. E. Mallouk, Understanding the efficiency of autonomous nano- and microscale motors. *J. Am. Chem. Soc.* **135**, 10557–10565 (2013).
47. I. S. Metcalfe, B. Ray, C. Dejoie, W. Hu, C. de Leeuwe, C. Dueso, F. R. García-García, C.-M. Mak, E. I. Papaioannou, C. R. Thompson, J. S. O. Evans, Overcoming chemical equilibrium limitations using a thermodynamically reversible chemical reactor. *Nat. Chem.* **11**, 638–643 (2019).
48. C. H. Bennett, R. Landauer, The fundamental physical limits of computation. *Sci. Am.* **253**, 48–56 (1985).
49. M. Konopik, T. Korten, E. Lutz, H. Linke, Fundamental energy cost of finite-time computing. arXiv:2101.07075 [cond-mat.stat-mech] (18 January 2021).
50. A. Ramaiya, B. Roy, M. Bugiel, E. Schäffer, Kinesin rotates unidirectionally and generates torque while walking on microtubules. *Proc. Natl. Acad. Sci.* **114**, 10894–10899 (2017).
51. H. Hess, Self-assembly driven by molecular motors. *Soft Matter* **2**, 669–677 (2006).
52. M. Hagiya, A. Konagaya, S. Kobayashi, H. Saito, S. Murata, Molecular robots with sensors and intelligence. *Acc. Chem. Res.* **47**, 1681–1690 (2014).
53. "Robot." (n. 2a) Merriam-Webster.com Dictionary, Merriam-Webster, www.merriam-webster.com/dictionary/robot [accessed 2 August 2021].
54. A. C. Balazs, P. Fischer, A. Sen, Intelligent nano/micromotors: Using free energy to fabricate organized systems driven far from equilibrium. *Acc. Chem. Res.* **51**, 2979–2979 (2018).
55. S. Collins, A. Ruina, R. Tedrake, M. Wisse, Efficient bipedal robots based on passive-dynamic walkers. *Science* **307**, 1082–1085 (2005).
56. E. Roldan, I. A. Martinez, J. M. R. Parrondo, D. Petrov, Universal features in the energetics of symmetry breaking. *Nat. Phys.* **10**, 457–461 (2014).
57. M. Held, O. Kašpar, C. Edwards, D. V. Nicolau, Intracellular mechanisms of fungal space searching in microenvironments. *Proc. Natl. Acad. Sci.* **116**, 13543–13552 (2019).
58. M. Rubenstein, C. Ahler, R. Nagpal, Kilobot: A low cost scalable robot system for collective behaviors, in *Proceedings of the 2012 IEEE International Conference on Robotics and Automation* (IEEE, 2012), pp. 3293–3298.
59. J. F. Boudet, J. Lintuvuori, C. Lacouture, T. Barois, A. Deblais, K. Xie, S. Cassagnere, B. Tregon, D. B. Brückner, J. C. Baret, H. Kellay, From collections of independent, mindless robots to flexible, mobile, and directional superstructures. *Sci. Robot.* **6**, eabd0272 (2021).
60. N. Napp, S. Burden, E. Klavins, Setpoint regulation for stochastically interacting robots. *Auton. Robot.* **30**, 57–71 (2011).
61. S. Chaudhuri, T. Korten, S. Korten, G. Milani, T. Lana, G. te Kronnie, S. Diez, Label-free detection of microvesicles and proteins by the bundling of gliding microtubules. *Nano Lett.* **18**, 117–123 (2017).
62. P. Katira, H. Hess, Two-stage capture employing active transport enables sensitive and fast biosensors. *Nano Lett.* **10**, 567–572 (2010).

63. D. Scalise, R. Schulman, Controlling matter at the molecular scale with DNA circuits. *Annu. Rev. Biomed. Eng.* **21**, 469–493 (2019).
64. H. Hess, J. Clemmens, C. Brunner, R. Doot, S. Luna, K.-H. Ernst, V. Vogel, Molecular self-assembly of "Nanowires" and "Nanospools" using active transport. *Nano Lett.* **5**, 629–633 (2005).
65. A. T. Lam, C. Curschellas, D. Krovvidi, H. Hess, Controlling self-assembly of microtubule spools via kinesin motor density. *Soft Matter* **10**, 8731–8736 (2014).
66. M. A. Huffman, A. Fryszkowska, O. Alvizo, M. Borra-Garske, K. R. Campos, K. A. Canada, P. N. Devine, D. Duan, J. H. Forstater, S. T. Grosser, H. M. Halsey, G. J. Hughes, J. Jo, L. A. Joyce, J. N. Kolev, J. Liang, K. M. Maloney, B. F. Mann, N. M. Marshall, M. M. Laughlin, J. C. Moore, G. S. Murphy, C. C. Nawrat, J. Nazor, S. Novick, N. R. Patel, A. Rodriguez-Granillo, S. A. Robaire, E. C. Sherer, M. D. Truppo, A. M. Whittaker, D. Verma, L. Xiao, Y. Xu, H. Yang, Design of an in vitro biocatalytic cascade for the manufacture of islatravir. *Science* **366**, 1255–1259 (2019).
67. H. Jia, P. Schwille, Bottom-up synthetic biology: Reconstitution in space and time. *Curr. Opin. Biotechnol.* **60**, 179–187 (2019).
68. T. Schwander, L. S. von Borzyskowski, S. Burgener, N. S. Cortina, T. J. Erb, A synthetic pathway for the fixation of carbon dioxide in vitro. *Science* **354**, 900–904 (2016).
69. D. L. Coy, M. Wagenbach, J. Howard, Kinesin takes one 8-nm step for each ATP that it hydrolyzes. *J. Biol. Chem.* **274**, 3667–3671 (1999).
70. M. C. Grant, S. P. Boyd, in *Recent Advances in Learning and Control* (Springer, 2008), pp. 95-110.
71. M. Grant, S. Boyd, CVX: MATLAB software for disciplined convex programming, version 2.0 beta (2013), (available at http://cvxr.com/cvx).

Acknowledgments: We thank N. Bassir Kazeruni for technical support; G. Bachand for providing the kinesin protein; and R. Tahvildari, D. Berard, R. Berti, and S. Leslie from McGill University and ScopeSys Inc. (supported by an NSERC Idea to Innovation Phase2B grant) for technical support related to the CLiC device. **Funding:** The authors gratefully acknowledge financial support from the National Science Foundation Division of Materials Research grant no. 1807514. This work was performed, in part, at the Center for Integrated Nanotechnologies, an Office of Science User Facility operated for the U.S. Department of Energy (DOE) Office of Science by Los Alamos National Laboratory (contract no. DE-AC52-06NA25396) and Sandia National Laboratories (contract no. 97 DE-AC04-94AL85000). **Author contributions:** Conceptualization: G.S. and H.H. Methodology: G.S. and H.H. Experiments and analysis: G.S. Simulations: S.T. Funding acquisition: H.H. Supervision: H.H. Writing (original draft): G.S. and H.H. Writing (review and editing): G.S., S.T., P.K., and H.H. **Competing interests:** The authors declare that they have no competing interests. **Data and materials availability:** All data are available in the main text or the Supplementary Materials. The MATLAB scripts used to analyze the data and perform the simulations are available at the Columbia Academic Commons Repository at https://doi.org/10.7916/d8-s96s-s556.

Submitted 28 May 2021
Accepted 4 October 2021
Published 3 November 2021
10.1126/scirobotics.abj7200

Science Robotics

Robotic end-to-end fusion of microtubules powered by kinesin

Gadiel Saper, Stanislav Tsitkov, Parag Katira, and Henry Hess

Sci. Robot. **6** (60), eabj7200. DOI: 10.1126/scirobotics.abj7200

Science Robotics (ISSN 2470-9476) is published by the American Association for the Advancement of Science. 1200 New York Avenue NW, Washington, DC 20005. The title *Science Robotics* is a registered trademark of AAAS.